remote sensing

MDPI

Article

The InflateSAR Campaign: Developing Refugee Vessel Detection Capabilities with Polarimetric SAR

Peter Lanz [1,2,*], Armando Marino [3], Morgan David Simpson [3], Thomas Brinkhoff [2], Frank Köster [1,4] and Matthias Möller [5]

1 Department of Computing Science, Carl von Ossietzky University of Oldenburg, Ammerländer Heerstraße 114-118, 26129 Oldenburg, Germany
2 Institute for Applied Photogrammetry and Geoinformatics, Jade University Oldenburg, Ofener Str. 16/19, 26121 Oldenburg, Germany
3 Department of Biological and Environmental Sciences, University of Stirling, Stirling FK9 4LA, UK
4 Institute for AI Safety and Security, German Aerospace Center (DLR), Rathausallee 12, 53757 Sankt Augustin, Germany
5 Faculty for Humanities and Cultural Sciences, Otto-Friedrich-University of Bamberg, Am Kranen, 96045 Bamberg, Germany
* Correspondence: peter.lanz@uni-oldenburg.de

Abstract: In the efforts to mitigate the ongoing humanitarian crisis at the European sea borders, this work builds detection capabilities to help find refugee boats in distress. For this paper, we collected dual-pol and quad-pol synthetic aperture radar (SAR) data over a 12 m rubber inflatable in a test-bed lake near Berlin, Germany. To consider a real scenario, we prepared the vessel so that its backscattering emulated that of a vessel fully occupied with people. Further, we collected SAR imagery over the ocean with different sea states, categorized by incidence angle and by polarization. These were used to emulate the conditions for a vessel located in ocean waters. This setup enabled us to test nine well-known vessel-detection systems (VDS), to explore the capabilities of new detection algorithms and to benchmark different combinations of detectors (detector fusion) with respect to different sensor and scene parameters (e.g., the polarization, wind speed, wind direction and boat orientation). This analysis culminated in designing a system that is specifically tailored to accommodate different situations and sea states.

Keywords: polarimetry (PolSAR); constant false alarm rate (CFAR) detector; polarimetric detector; sub-look detector; vessel-detection system (VDS); ship detection; synthetic aperture radar (SAR); disaster mitigation, refugee boat

Citation: Lanz, P.; Marino, A.; Simpson, M.; Brinkhoff, T.; Köster, F.; Möller, M. The InflateSAR Campaign: Developing Refugee Vessel Detection Capabilities with Polarimetric SAR. *Remote Sens.* **2023**, *15*, 2008. https://doi.org/10.3390/rs15082008

Academic Editors: Magaly Koch, Zhixiang Fang, Yukiharu Hisaki, Jaroslaw Tęgowski and Quanyi Huang

Received: 2 March 2023
Revised: 31 March 2023
Accepted: 2 April 2023
Published: 10 April 2023

1. Introduction

The ongoing humanitarian crisis at Europe's southern maritime border has made it the world's deadliest border. For many years, migrants have been risking their lives to cross the Mediterranean Sea under very poor conditions on routes that are frequently controlled by human traffickers. Up-to-date and historic data and statistics about the maritime migration into Europe and its toll on human life can be found on the web services of the Missing Migrants Project [1], the International Organization for Migration [2] and the United Nations Refugee Agency [3].

Search and rescue organisations on the ground attempt to mitigate the impact of the continuously high numbers of maritime disasters, and one of the main hindrances is the difficulty of quickly locating migrant boats in distress. These operations use different strategies for maritime surveillance, such as vessels, airplanes and drones, and satellite-based search is another useful tool for this task. For such a time-critical application in disaster mitigation, synthetic aperture radar (SAR) is appropriate and practicable due to its all-weather and its 24 hour imaging capabilities. Moreover, the detection of ships and other maritime objects with SAR has a long research history (e.g., [4–11]).

With the rapid evolution in processing power, the pattern recognition community also added an important contribution to ship detection. However, many of the traditional methods, such as region selections, scale-invariant feature transform (SIFT), support vector machine (SVM) and histogram of oriented gradients (HOG), are typically associated with high computing costs. With deep learning, the time performance increases because it uses GPU acceleration. Different approaches using convolutional neural networks (CNN) began to evolve rapidly, and we see different deep-learning models for object detection (e.g., [12,13]) and image-classification tasks.

The region-based convolutional neural network (RCNN; [14]) and the sliding window were followed by Fast-RCNN [15] and Faster-RCNN [16,17]. Improvements and reduced complexity were achieved by using the softmax function instead of SVMs by using multiresolution convolutional features and by dividing the large detection area into region of interest (ROI) images. Ref. [18] used this approach for the detection of ships.

Ref. [19] presented a grid-CNN (G-CNN), which is a combination of a backbone-CNN (B-CNN) and a detection-CNN (D-CNN) to further improve and speed up automatic ship detection. Other approaches, such as YOLO [20] and YOLOv2, attempt to embrace the whole image during the training and testing period [21]. Ref. [22] used a deep neural network (DNN) for SAR image classification with the sliced Wasserstein distance (SWD) to provide a better solution to the optimization problem.

In our research, we attempt to adapt well-known detectors and develop detection capabilities with SAR for 12 m long rubber inflatables. This specific type of sea vehicle is predominantly used to cross the central Mediterranean Sea. In most cases, they are sent to the ocean packed with more than 100 passengers. Shorter versions of such boats (10 or 8 m long), but identical in construction, are used on other routes, for example in the Aegean Sea.

Our previous work on the development of automatic detectors for such migrant rubber boats was based on SAR data that we collected from an original 12 $\times$ 3.5 m inflatable [23]. Those data enabled us to examine the radar pattern of our special maritime vessel under different combinations of scene parameters (e.g., the incidence angle and resolution) and sensor parameters (e.g., the boat orientation) and to evaluate them for their impact on the detectability of the inflatable. We tested and compared a variety of existing automatic vessel detectors [24]. Our results are, we think, noteworthy and legitimate and offer significant insights regarding the behaviour of the inflatable when hit by microwaves and the interactions with the surrounding water surface. With this, we can detect the empty inflatable on a lake.

For this research, we collected data to create a more realistic scenario by simulating passengers on the vessel and combining this with SAR imagery from the ocean. This enabled us to analyse the SAR vessel-detection capabilities for migrant rubber inflatables for a variety of sensor settings and scene parameters, such as the wave height and wave direction. We present a polarimetric analysis of the backscattering behaviour of the fully occupied inflatable and benchmark a variety of well-known detectors with respect to several influencing parameters. To improve the detection quality, we experiment with new algorithms with adaptations of the Intensity Dual-Polarization Ratio Anomaly Detector (iDPolRAD) [25] and with the combination of detectors.

2. Materials and Methods

2.1. The Human Scattering Experiment

In this initial experiment, we evaluated which material was best suited to emulate the presence of humans on a rubber inflatable and was sufficiently durable to remain in the vessel on a lake for several months. During the whole campaign, the material properties that influence the scattering behaviour (roughness, shape, water content and dielectric property) must remain constant. With a mobile/handheld radar sensor, we compared the radar backscatter behaviour of a number of material with that of humans. The experiments involved:

- Four volunteers sitting close to each other on the ground of an empty room. We chose the sitting posture because that most closely resembles the real situation in the migrant inflatable. The data include different arrangements: four people in a row perpendicular to the sensor line of sight (LoS) ('H4×1'), two rows of two people behind each other ('H2×2') and all four people in one column behind each other parallel to the LoS ('H1×4').
- Water-soaked clay pebbles, packed in 30 × 40 cm air-tight plastic bags. The bags themselves are invisible to microwaves and the soaked clay pebbles, as they are roundish objects smaller than the wavelength and with a similar water content to the human body and, thus, should appear similar to the uppermost body parts (heads and shoulders). We took data from two bags perpendicular to the LoS ('C2×1'), two bags parallel to the LoS ('C1×2'), two bags sitting on top of each other ('C1×1×2') and two bags stacked with one large bag (30 × 60 cm) standing behind them ('C1×1×2+1').
- Steel wool clumped to random 20 cm diameter balls to imitate the top layer of passengers in a boat. The acquisitions involved six balls in two rows ('S2×3') and two balls plus four 5 × 10 × 60 cm (h,w,l) steel wool layers not clumped but stretched out in the front ('S2+4').

The dielectric constant ϵ' is an important factor during the interaction with electromagnetic waves. For a given shape, the lower the dielectric constant, the higher the backscatter intensity from volume scattering [26]. A very low dielectric constant, such as air or PVC (all dry) renders them almost invisible to microwaves and increases the penetration depth. The dielectric property is a function of the temperature and the microwave frequency and of course the exact composition of the particular material. Dry clay pebbles would be almost invisible to microwaves due to their very low ϵ' (Table 1). For that reason, we water-soaked the clay pebbles and used air-tight bags to preserve a similar water content to that of the human body (about 80%) throughout the acquisition campaign.

Table 1. The dielectric properties for a list of materials involved in our detection scenario at 20 °C (* at 37 °C) [27]. The value for sea water, given the typical salinity of the Mediterranean Sea, is about 38 g per kilo [28].

Material	Dielectric Constant ϵ'	Loss Tangent tan δ
Air	1	depends on weather
Blood *	58	0.27
Fat *	5.5	0.21
Muscle *	49	0.33
Nylon	2.4	0.0083
Polyethylene	2.25	-
Water, fresh [29]	80	-
Sea water [30,31]	70	-
Sea ice [26]	4	0.5
Sandy soil (dry)	2.55	0.0062
Clay bricks	3.7-4.5	-
Metals	infinite	-
Plywood	2.5	

The loss tangent is the relation between the dielectric constant ϵ' and the loss factor ϵ'' and describes the conductivity of a medium:

$$\tan(\delta) = \frac{\epsilon''}{\epsilon'} \tag{1}$$

The dielectric permittivity ϵ_c is defined as a complex number:

$$\epsilon_c = \epsilon' - i\epsilon'' \tag{2}$$

consisting of the dielectric constant (real) and the loss factor (imaginary). The latter describes the electromagnetic loss of a medium. A low electromagnetic loss generally results in an additional contribution from volume scattering [26].

Fresh water has an ϵ' similar to blood or muscle tissue, which justifies/explains our use of water-soaked clay pebbles. Steel wool has, as with all magnetic matter, a very high dielectric constant, and its ϵ_c is infinite. Due to that and due to its shape, we expect it to behave similarly to human bodies and to have a strong volume backscattering signal.

Figure 1 compares the intensity images of all three test cases. The test objects are placed at the same distance from the sensor (y-axis) whereas the x-axis represents the number of pulses. In this case, 65 consecutive pulses were emitted and recorded. The radar return from H2×2 is speckled in time due to movement, and the signal is more spread out since human bodies occupy a wider space along the LoS than the comparably small test objects (Figure 1, left). The wall in the background is more clearly visible in the scenarios with clay pebbles and steel wool since the objects used are much smaller than four people, occupy much less space and produce less occlusion (Figure 1, centre and right). To evaluate how many sacks are needed, we summed up the intensity values of all pulses of the different materials and the humans within each scenario. The comparison of these backscattering intensities revealed that approximately 90 bags of soaked clay would emulate 80 occupants.

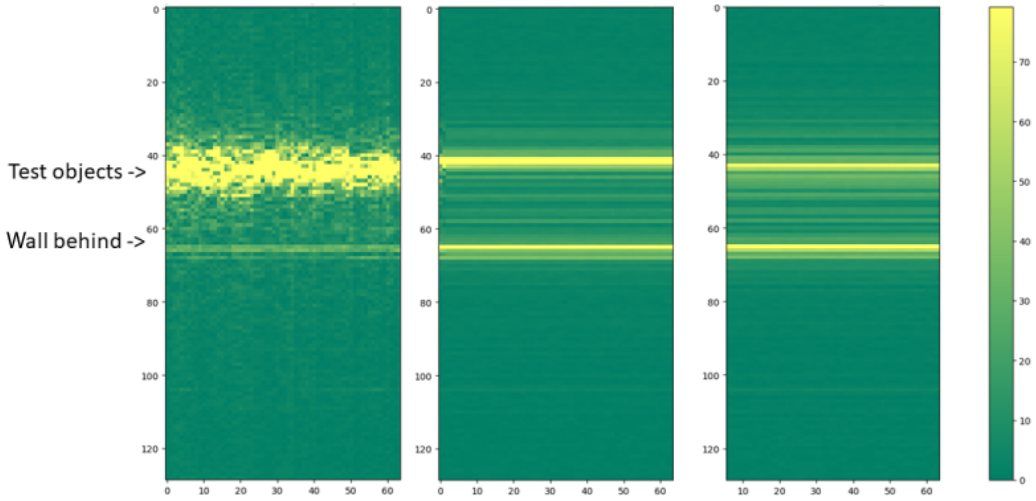

Figure 1. Example results (in dB) of the human backscattering experiments: H2×2 (**left**), C2×2×2 (**centre**) and S2×3 (**right**). The y-axes show the distance from the sensor in decimetres.

2.2. Data Campaign and Data Collection

We set up the data campaign on a small lake in northern Germany in spring 2022. The test object was a 12 × 3 m rubber (1.2 mm PVC) inflatable with a wooden floor and no metal parts at all.

Due to its dielectric properties, the boat itself is expected to be hardly visible using microwaves (see Table 1; [23]). Finally, we placed 90 bags of soaked clay pebbles in a way that makes them cover the whole area of the vessel, including the inflated volumes that passengers use to sit on (Figure 2).

(**a**) Top view (**b**) Side view

Figure 2. SAR data acquisition setup in the test-bed lake.

We expected the bags to leave a similar radar signature compared to a group of 80 people sitting in the boat. First, the bags were expected to simulate the volumetric structure created by many people with their shoulders and heads placed close to each other. Second, the water in the volume-like clay pebbles, preserved over the whole time by air-tight bags, should resemble the water content of the human body. Our approach to simulate the backscattering of a human body in different frequencies is supported by similar studies. For example, Ref. [32] used wet sand for Ultra Wide Band (UWB) radar. In our experiment, we expect a stronger intensity signature compared to an empty boat (see [24]).

Thus, prepared, the boat sat on the lake perpendicular to the LoS (in a N-S direction) for the first two months. In a second phase, we oriented it at 45° to the LoS and acquired data for another two months. These two geometries should represent two diametrically different scenarios when it comes to scattering mechanisms. The boat oriented 90° relative to the LoS should generate a strong radar backscattering since it exposes the maximum amount of surfaces facing the LoS and being capable of scattering the EM-waves directly back through double reflections [23]. The boat oriented at 45°, on the other hand, is expected to scatter some of the multiple reflections away from the sensor. This is because the volume scattering expected by the human-equivalent and from the vessel facets (for example in case they are wet) is not fully isotropic.

The data collected comprise full-pol data from Cosmo-SkyMed Second Generation (CSG), dual-pol Stripmap data in several combinations from TerraSAR-X (TSX) and very high-resolution VV-pol data from ICEYE (Table 2).

Table 2. Overview of the data collected for the boat on the lake with 80 simulated people.

Mission	Mode	Average Pixel Size (m²)	Polarization	Incidence Angle	Datasets
TerraSAR-X	Stripmap	4.4	Dual-pol: HH VV, HV HH, VH VV	Low, medium and high	46
Cosmo-SkyMed	Spotlight	2.7	Quad-Pol	Medium and high	4
ICEYE	High-res. Spotlight	0.6	Single-Pol: VV	Low and medium	4

For the CSG and the TSX data, we attempted to cover different combinations of sensor and scene setting, such as incidence angle, dual-pol polarization and the orientation of the boat. This enabled us to analyse the influence of these parameters on the scattering behaviour of the inflatable and on the performance of the detectors.

Table 3 quantifies the available TSX datasets. The categories for the incidence angles are defined as smaller than 28° for 'low', from 28° to 43° for 'medium' and greater than 43° for 'high'. The figures list the datasets where an unambiguous identification of the boat on the lake was possible; figures in brackets represent unsuccessful identifications. The reason

for the latter was mainly strong Bragg scattering due to low incidence angles. We speak of an unambiguous identification when the target-to-clutter ratio (TCR) of at least one of the polarization channels is larger than three times the clutter standard deviation σ in dB:

$$TCR \geq 3 * \sigma_{clutter} \tag{3}$$

where TCR is defined as the ratio between the maximum backscattering of the rubber inflatable and the mean of the backscattering of the local lake clutter. In dB, the ratio has a difference. It is useful to express σ^0 in the decibel (dB) scale since it can be statistically modelled with a Gaussian distribution. In linear scale, the fit of a generalized gamma distribution would be much more appropriate and (3) would have to be adapted accordingly.

Table 3. TSX data parameter matrix of the 'full' inflatable on the lake.

	90 Degrees			45 Degrees		
	Low	**Medium**	**High**	**Low**	**Medium**	**High**
HH VV	1 (1)	4	3	3 (2)	5	5
HV HH	1	2	2	1 (1)	3	2
VH VV	1	2	1	1 (1)	2	2

The high variability of the ocean surface due to wind speed, wind direction, swell and other factors has grave implications for its scattering behaviour. The backscattering intensity changes with the water wave height, frequency, form and orientation relative to the LoS of the radar. Moreover, the combination of scattering mechanisms changes with the existence and density of wave features, such as foam or breaking waves [33–37]. Consequently, higher sea states are expected to hamper the detection task.

Figure 3a visualizes an example for the increased radar backscattering intensity from 2.1 m waves. On the right, the corresponding detection probability map from the intensity-based cell averaging-constant false alarm rate (CA-CFAR) detector shows how the waves can raise the false positive rate.

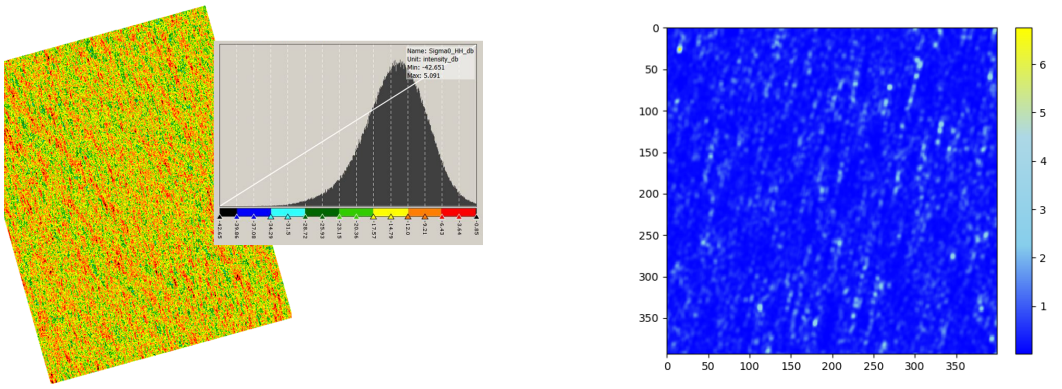

(**a**) (**b**)

Figure 3. Radar signature of 2.1 m waves in the up/down direction, HH-pol and TSX Stripmap (left) and its implications for the detection task (right) (@ DLR 2014). (**a**) Radar signature (σ^0 in dB); (**b**) CA-CFAR probability map. Axis labels are in meters.

To analyse and quantify the influence of the significant wave height H_s on the performance of the detectors, we gathered a collection of SAR data from the ocean. These ocean data comprise different H_s for a selection of combinations of wave directions, incidence angles and dual-pol combinations. We arranged our collection classifying the wave direction (relative to the LoS) in two groups:

- Cross-wind waves: these are waves that move perpendicular to the LoS. They move in the direction of the satellite azimuth, which is close to N-S.

- Up/down-wind waves: here, the waves move in the range direction.

The wave direction is—particularly for low wind speed/low waves—an important impact factor for the backscattering behaviour of the water surface (e.g., [38]). The LoS was calculated using the heading of the satellite defined by the azimuth angle, which is 10.2° for TSX. That means a heading of 349.8° for ascending orbits and 190.1° for descending orbits. We accepted an average deviation of 10° between the wave direction and the respective directions for up/down wind and cross wind.

We determined the wave direction and H_s of the TSX-archive datasets with the help of in situ wave-sensor buoys from the Copernicus Marine Environment Monitoring Service In Situ Thematic Assembly Centre (CMEMS In Situ TAC). In fact, we only used SAR data near in situ buoys where the wave height and wave direction data were available. To verify the data, we double checked the plausibility with data from nearby buoys of that network and with estimations from a number of Copernicus wave models covering different ocean areas:

- North Sea: Atlantic–European North-West Shelf-Wave Physics Reanalysis.
- Mediterranean Sea and West Gibraltar region: Mediterranean Sea Waves Reanalysis.
- Arctic Ocean: Arctic Ocean Wave Hindcast.
- All other maritime regions not covered by a high-resolution wave model: Global Ocean Waves Reanalysis WAVERYS.

From these models, we extracted and used parameters, such as the *sea surface wave significant height (VHM0 or Hm0 (m))*, *significant height of waves Hs on the water body (VGHS (m))* and *average height highest wave (VAVH)* for the wave height, *wave principal direction at spectral peak (VPED)*, *direction from which the waves are coming relative to true north (VDIR)*, *direction from which the wind is coming relative to true north (WDIR)* and *the wave-induced horizontal Eulerian mean current (HCDT)*, to determine the main direction of the waves. The latter is useful since the Eulerian mean current is always in the direction of the waves [39].

We followed the Beaufort scale (BFT) to define our wave height categories in Table 4, and each category corresponds to a specific sea state defined in that scale. This collection enables us to examine the impact of a variety of sea states on the radar backscattering and on the detection task. As Table 4 shows, the collection of ocean data was subdivided according to the polarization, the incidence angle (low, medium and high) and the principal wave direction relative to the LoS (up/down and cross).

Table 4. Collection of TSX dual-pol ocean data covering different wave directions, wave heights, polarimetric channel combinations and incidence angles.

Polarization		**HH VV**			**HV HH**		**VH VV**	
Incidence Angle	**Low**	**Low**	**Medium**	**High**	**Medium**	**High**	**Medium**	**High**
Wave Direction	**Cross**	**Up/Down**	**Up/Down**	**Up/Down**	**Up/Down**	**Up/Down**	**Up/Down**	**Up/Down**
Wave Height (m)								
0.4–0.8 (BFT3)	✓	✓	✓	✓	✓	✓	✓	✓
0.8–1.5 (BFT4)	✓	✓	✓	✓	✓		✓	✓
1.5–2.5 (BFT5)		✓			✓	✓	✓	✓
2.5–3.5 (BFT6)			✓	✓				
3.5–4.5 (BFT7)						✓		
4.5–6.5 (BFT8)	✓							

Figure 4 provides an overview of our collection of TSX archive SAR data of different wave heights and the water surface mean backscattering energy by polarization. The acquisitions from the lake test bed are included as well ($H_s = 0$). It shows a general trend of stronger backscattering from the water surface with increasing H_s. Moreover, small incidence angles tend to give very high backscattering intensities due to larger Bragg scattering. In co-pol datasets, VV shows a slightly higher mean intensity value throughout the data collection (HH: −15.5 dB and VV: −14.4 dB). At medium and high incidence angles, the return from the water surface is very low—especially for cross-pol channels.

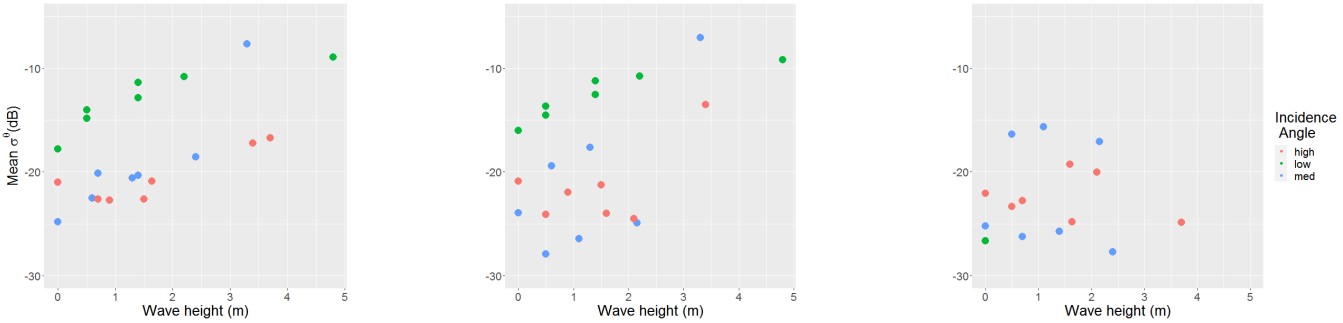

(**a**) HH-pol. (**b**) VV-pol. (**c**) Cross-pol (HV or VH).

Figure 4. TSX dual-pol data collection of different wave heights and their mean backscattering intensity; one diagram for each polarization.

To facilitate the testing of vessel detector algorithms at different sea states, we fused the simulated 'full' inflatable with the datasets showing the ocean. All important sensor parameters (resolution/acquisition mode, incidence angle and polarization), were considered, and we replaced pixels in the images from the ocean with the pixels of the boat. The pixels of the boat on the lake were chosen using an intensity-based approach as described in Formula (3). Figure 5 shows a ground truth map with four different signatures of the inflatable (yellow) inserted at random positions into the ocean data (purple). This binary mask with yellow pixels represent the 'positive true' case in the following analysis. Again, we took extra care to only replace pixels where the satellite parameters were similar.

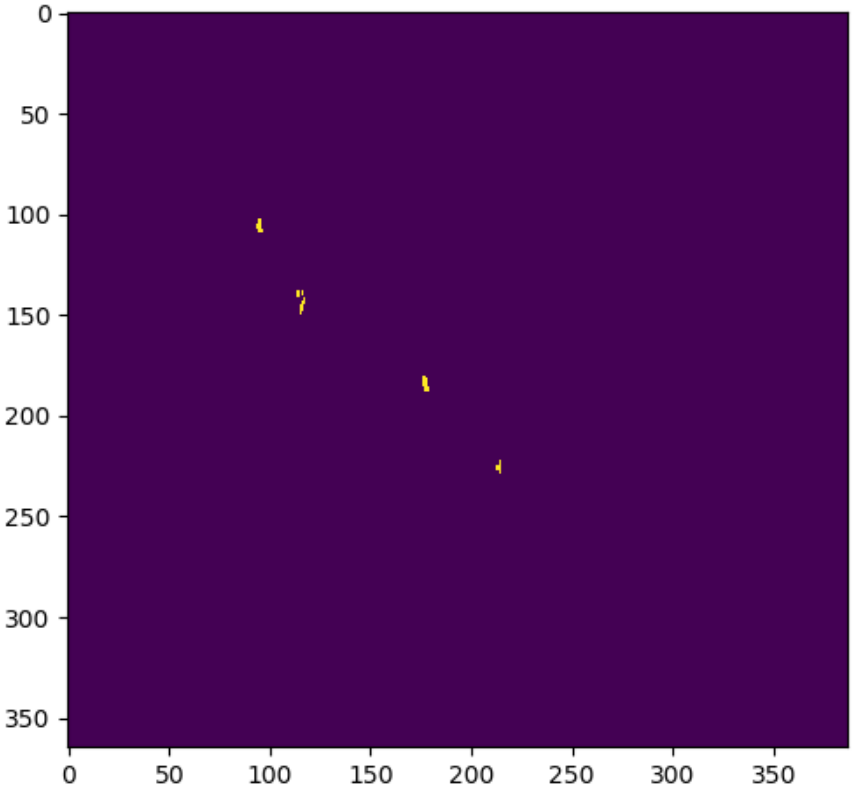

Figure 5. A 350 × 350 m ground truth map after insertion of the positive true pixels (yellow) of four different acquisitions from the rubber inflatable. Purple pixels represent the ocean surface.

2.3. Polarimetric Analysis of the Inflatable

Decomposition theorems (DT) provide a physical interpretation of the signals scattered from a target by considering them as a combination of several components. To better

understand the scattering mechanisms at the inflatable, we used quad-pol CSG data for a selection of well-known coherent and incoherent polarimetric decompositions as listed in Table 5. In this context, the term *coherent* indicates the decomposition of the scattering matrix [S] (Pauli, Cameron), including the phase information, whereas incoherent decompositions (Yamaguchi, Cloude–Pottier) use the averaging coherency [C] or covariance [(]T] matrix [40].

The most commonly known coherent model-based decomposition is the Pauli decomposition where the scattering matrix [S] is the sum of the complex quantities of odd-bounce (e.g., single bounce), even-bounce (e.g., double bounce) and 45° rotated double bounce (see Table 5). The Cloude–Pottier decomposition or Entropy/Anisotropy/Alpha decomposition (H/A/$\underline{\alpha}$) [41,42] proposes the existence of three orthogonal scattering mechanisms. It belongs to the category of eigenvector-based TDs and is especially useful for partial targets. To retrieve its parameters, it is necessary to form the covariance matrix in the Pauli basis.

Working on the assumption of a monostatic system and reciprocity, the Pauli vector is $k_p = \frac{1}{\sqrt{2}}[HH + VV, HH - VV, 2 * HV]^T$. This matrix is then called coherency matrix [T]. In the quad-pol reciprocal scenario, [T] gives three independent scattering mechanisms along its main axis: surface scattering $T_{11} = \langle \underline{k}_1 \underline{k}_1^{*T} \rangle$, double-bounce scattering $T_{22} = \langle \underline{k}_2 \underline{k}_2^{*T} \rangle$ and volume scattering $T_{33} = \langle \underline{k}_3 \underline{k}_3^{*T} \rangle$. The three roll-invariant parameters H, A and $\underline{\alpha}$ can be used to describe the quantitative proportion between the three scattering mechanisms. For our detection task, H was found to be particularly useful.

Table 5. Polarimetric decompositions and parameters. The Yamaguchi parameters had their orientation removed.

Parameter	Decomposition	Note
Alpha	Cloude–Pottier	
Entropy	Cloude–Pottier	
Single Bounce	Yamaguchi Y4R	
Double Bounce	Yamaguchi Y4R	
Volume Scattering	Yamaguchi Y4R	
Helix Scattering	Yamaguchi Y4R	
Symmetry	Yamaguchi Y4R	Huynen Target Generator A0
Irregularity/Double Bounce	Yamaguchi Y4R	Huynen Target Generator B0-B
Non-symmetry	Yamaguchi Y4R	Huynen Target Generator B0+B
Even bounce	Pauli	|HH-VV|
Even bounce 45° oriented	Pauli	|HV|
Odd bounce	Pauli	|HH+VV|
Trihedral	Cameron	
Dipole	Cameron	
Narrow Diplane	Cameron	
Diplane	Cameron	
Left Helix	Cameron	
Right Helix	Cameron	
Cylinder	Cameron	
1/4 Wave Device	Cameron	

The model-based Yamaguchi decomposition [43] added the helix parameter to the Freeman and Durden decomposition [44], adding an asymmetric component to the scattering model. Helix scattering is fully determined by the imaginary part of the T_{23} element of the coherency matrix. This element is expected to be strong when there is no reflection symmetry, such as in forests or 45° oriented built-up areas.

It is expected to be weak for flat surfaces and parallel built-up areas. Polarimetric reflection symmetry means there is no correlation between the co-pol and the cross-pol channels [45]:

$$\langle S_{HH} S_{HV}^* \rangle = \langle S_{HV} S_{VV}^* \rangle = 0 \quad (4)$$

The Cameron decomposition [46] uses the Pauli spin matrices to decompose and to classify [S] in several steps. The scattering [S] matrix is described as the complex sum of these basis matrices. Each of them is associated with one of the elementary scattering mechanisms: single scattering from plane surfaces, diplane scattering from corner reflectors oriented 45° and non-symmetric components. The Cameron decomposition is a multistage procedure.

First, the degree of reciprocity (in Cameron's formula the angle θ) is calculated in order to examine whether the reciprocal components dominate or not by separating the symmetric and non-symmetric parts. For the scattering matrix of reciprocal objects, the elements S_{12} and S_{21} are equal. If the reciprocal part is dominant, the reciprocal term is decomposed into symmetric and asymmetric scatterers. Representative [S] matrices for asymmetric left and right helices are:

- Left helix: $S_{hl} = \frac{1}{2}\begin{bmatrix} 1 & i \\ i & -1 \end{bmatrix}$
- Right helix: $S_{hr} = \frac{1}{2}\begin{bmatrix} 1 & -i \\ -i & -1 \end{bmatrix}$

If the [S] matrix exhibits asymmetry, its share of left helix and right helix is calculated. In a final step, if the matrix is symmetric, it is compared to a list of symmetric scatterers.

- Trihedral: $\frac{1}{\sqrt{2}}\begin{bmatrix} 1 & 0 \\ 0 & 1 \end{bmatrix}$
- Diplane: $\frac{1}{\sqrt{2}}\begin{bmatrix} 1 & 0 \\ 0 & -1 \end{bmatrix}$
- Dipole: $\begin{bmatrix} 1 & 0 \\ 0 & 0 \end{bmatrix}$
- Cylinder: $\frac{1}{\sqrt{5}}\begin{bmatrix} 2 & 0 \\ 0 & 1 \end{bmatrix}$
- Narrow diplane: $\frac{1}{\sqrt{5}}\begin{bmatrix} 2 & 0 \\ 0 & -1 \end{bmatrix}$
- 1/4 wave device: $\frac{1}{\sqrt{2}}\begin{bmatrix} 1 & 0 \\ 0 & i \end{bmatrix}$

where, according to Cameron, a symmetric scatterer has an axis of symmetry in the plane of the radar line of sight (LoS).

The Cameron decomposition is a coherent DT, such as, for example, the Krogager decomposition [47]. This group of DTs are particularly useful in the case of one dominant scattering mechanism. Cameron's cylinder and narrow diplane scattering can be composed of trihedral, dihedral and dipole scattering. Together with the quarter wave device, they can be called fundamental scattering mechanisms [48].

2.4. Detector Comparison and Detector Fusion

We tested and benchmarked nine different vessel-detection systems (VDS; Table 6) algorithms using receiver operating characteristic (ROC) curves. ROC curves are plots of the probability of detection (P_d) versus the probability of false alarm (P_{fa}). To quantify and compare the results from the ROC curves, we estimated the area under the curve (AUC) and grouped them for different wave heights and detectors.

ROC curves are computed by varying the threshold between a minimum and a maximum value depending on the histogram of the detector output. The AUC is a value for the classifier's performance: an AUC of 1 is the best achievable result and means 100% detection with no false alarms. An AUC of 0.5 is obtained for detectors making random choices. All VDS were implemented using a sliding window of a specific size (CUT) with a guard window around it and a training window around the guard window.

Table 6. Overview of the vessel-detection algorithms being tested and their parameterization.

Detector	Cells Under Test (CUT) Window Size	Guard Window Size	Train Window Size
Polarimetric Symmetry Detector (PolSym)	1	2	5
Polarimetric Notch Filter (PNF)	5	12	36
Polarimetric Entropy Detector (PolEntropy)	2	-	10
Polarimetric Match Filter (PMF)	5	12	36
Intensity Depolarization Ratio Anomaly Detector (iDPolRAD)	1	12	36
Surface Intensity Depolarization Ratio Anomaly Detector (SiDPolRAD)	1	12	36
Sub-look Correlation Detector (SubCorr)	1	-	36
Polarimetric Whitening Filter (PWF)	5	12	36
Cell Averaging Constant False Alarm Rate (CA-CFAR)	1	24	36

During a preliminary phase of benchmarking and detector tuning, we selected, for each detector, the parameterization that translates into the best performance (Table 6). PolEntropy and the SubCorr worked better without a guarding window, so we removed it for those two. The iDPolRAD is actually intended for use as a volume detector and designed to work with the cross–polarization over co–polarization ratio [25].

Since we applied it to all available combinations of dual-pol data, including HH VV, we refer to it here as PolRatio1 when used with cross-pol data and PolRatio3 when used with co-pol data. The same is true for its surface and double-bounce scattering detecting variant SiDPolRAD [24], which we rename as PolRatio2 when used with cross-pol data and PolRatio4 when used with co-pol data. For VH VV and HV HH, the two detectors are defined as:

$$PolRatio1: \frac{\langle|cross\text{-}pol|^2\rangle_{test} - \langle|cross\text{-}pol|^2\rangle_{train}}{\langle|co\text{-}pol|^2\rangle_{train}} * \langle|cross\text{-}pol|^2\rangle_{test} \quad (5)$$

$$PolRatio2: \frac{\langle|co\text{-}pol|^2\rangle_{test} - \langle|co\text{-}pol|^2\rangle_{train}}{\langle|cross\text{-}pol|^2\rangle_{train}} * \langle|co\text{-}pol|^2\rangle_{test} \quad (6)$$

Applying those two to the HH VV polarization combination, we express them as:

$$PolRatio3: \frac{\langle|HH|^2\rangle_{test} - \langle|HH|^2\rangle_{train}}{\langle|VV|^2\rangle_{train}} * \langle|HH|^2\rangle_{test} \quad (7)$$

$$PolRatio4: \frac{\langle|VV|^2\rangle_{test} - \langle|VV|^2\rangle_{train}}{\langle|HH|^2\rangle_{train}} * \langle|VV|^2\rangle_{test} \quad (8)$$

A possible physical interpretation for PolRatio3 is 'dihedral scattering' since the HH channel is stronger compared to the VV channel when we have a horizontal dihedral. The interpretation for PolRatio4 is 'Bragg scattering' since VV is stronger than HH in the case of Bragg scattering.

At this point, we were able to identify the most promising detectors for each dual-pol combination of polarimetric channels against the background of different wave heights. To

improve the detection capabilities for our vessel, we tested different combinations of the top ranking detectors.

Each detector produces a detection probability map. This map is then classified by applying a threshold to generate the detection mask. This mask is a binary image showing the detector decision at a specific threshold. Each pixel receives either a zero value for 'no boat' or a one value for 'boat detected'. To fuse binary detection masks coming from different detectors, we tested different combinations of the logical operators 'OR' and 'AND' (Figure 6). Further, we tested detection algorithms that use the intensity and the ratio between the T_{11} (surface scattering), T_{12} (compound H– and V–dipoles, [49]) and T_{22} (double-bounce scattering) elements of the covariance matrix. The double-bounce scattering can come from the side of the inflatable and the passengers inside, which, together with the water surface, form dihedral structures. The term T_{22} can be expanded as:

$$T_{22} = \frac{1}{2}\langle|S_{HH} - S_{VV}|^2\rangle = \frac{1}{2}\langle|S_{HH}|^2\rangle + \frac{1}{2}\langle|S_{VV}|^2\rangle - \langle Re\{S_{HH}S_{VV}^*\}\rangle \quad (9)$$

In the dihedral scattering, the most significant feature is that the co-polarized components HH and VV are in opposite phase. Therefore, T_{22} increases to the maximum when the last part of Equation 9 becomes smaller than zero.

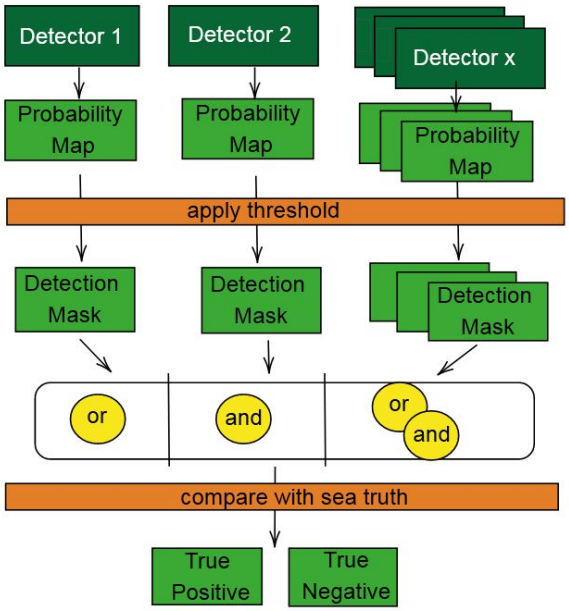

Figure 6. Detector melange flow diagram.

3. Results

3.1. Qualitative Inspection of High Resolution Data

At this point, we present three high-resolution spotlight images from ICEYE. These single-VV-pol images provide insight into the location and spatial variation of scattering mechanisms producing the radar backscattering of the rubber inflatable.

Figure 7 shows the boat with different sensor parameters at a sub-metre resolution of about 0.8 m. All three allow for a good visual identification and a precise size estimation. Strong scattering responses (bright pixels) are almost uniformly spread throughout the vessel. At a low incidence angle (Figure 7a), the mean response from the water surface is at about 10 dB and, compared to higher incidence angles, is increased by Bragg scattering. The vessel response is stronger as well; however, that increase is less strong. The wave structure of the water seems to be disturbed by the boat in the southeast–northwest direction, where there are also areas of lower backscattering.

This theory is backed by recordings from the Deutsche Wetterdienst (DWD) of the wind direction being 330° at the time of acquisition. At medium incidence angles, the mean radar response from the water surface (Figure 7b,c) is around 16 dB, and the TCR is higher. The vessel orientation relative to the LoS is clearly visible.

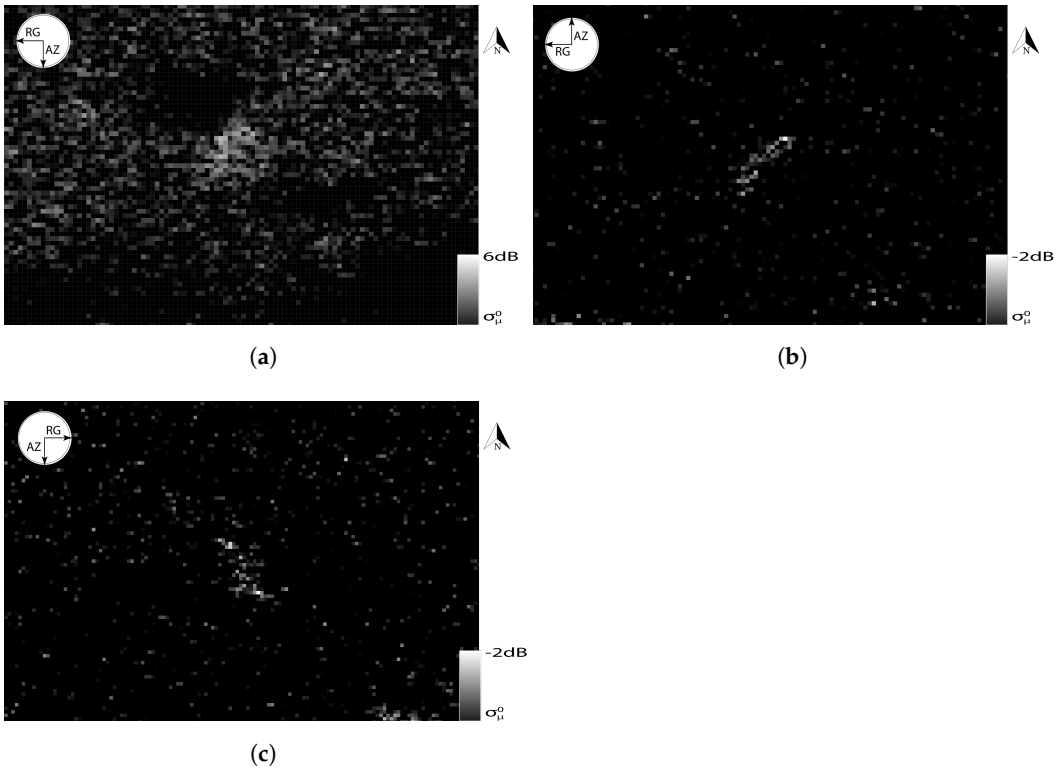

Figure 7. High-resolution ICEYE VV-pol of the vessel at different wave heights and their mean backscattering intensity. μ = mean of the water surface backscattering, σ = standard deviation of the water surface backscattering (@ ESA 2022). (**a**) Low incidence angle, 45° inclined boat. (**b**) Medium incidence angle, 45° inclined boat. (**c**) Medium incidence angle, orthogonal boat.

3.2. Polarimetric Scattering Analysis

A pixel-wise Pauli RGB image analysis (Figure 8) shows that the boat triggers different scattering mechanisms. For the filtering of [C] and [T] matrices, we used a rather small 3×3 window to preserve the spatial resolution as much as possible.

Table 7 lists the contributions of scattering mechanisms according to the Pauli decomposition. Double-bounce and single-bounce scattering clearly dominate. Volume scattering plays a minor role across the range of different acquisition parameters and seems to be stronger at low incidence angles.

Table 7. Pauli scattering mechanisms (dimensionless, comparative quantities, normalized to 0->1).

	Double Bounce	Volume	Single Bounce
low inc. angle, inclined vessel	0.41	0.25	0.41
low inc. angle, orthogonal vessel	0.33	0.17	0.33
medium inc. angle, orthogonal vessel	0.68	0.26	0.73

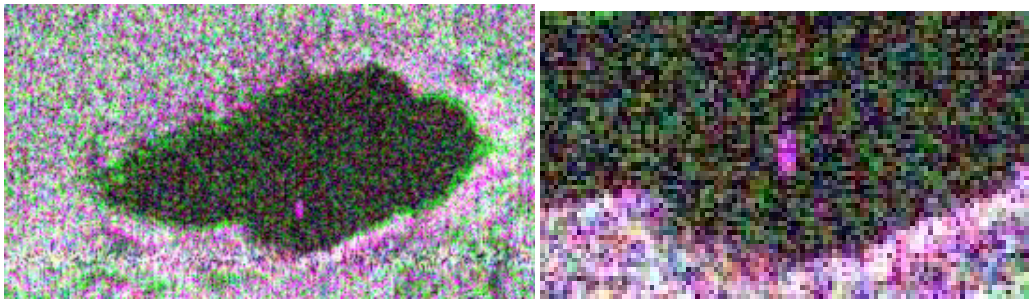

(**a**) (**b**)

Figure 8. Pauli R (double bounce) G (volume scattering) B (single bounce) composites for the orthogonal vessel at a medium incidence angle (@ ASI 2022). (**a**) Pauli RGB from the lake test bed. (**b**) Pauli RGB from a section of the lake with the rubber inflatable in the centre.

The Cloude–Pottier decomposition delivers low entropy at low incidence angles and medium entropy for medium incidence angles (Table 8, Figure 9). The mean alpha angle varies throughout the three acquisitions, indicating a dominance of surface scattering and double-bounce scattering as well as minor contributions from volume scattering.

Table 8. The results of the Cloude–Pottier decomposition of the inflatable (dimensionless, comparative quantities, normalized to 0->1).

	H	Mean Alpha
Low inc. angle, inclined vessel	0.46	0.32
Low inc. angle, orthogonal vessel	0.46	0.65
Medium inc. angle, orthogonal vessel	0.58	0.54

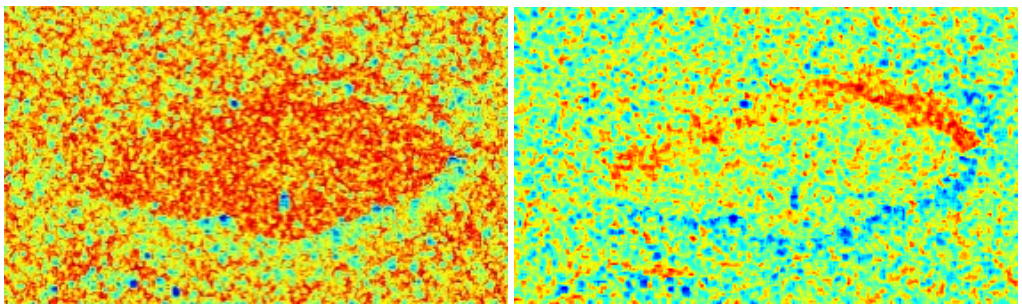

(**a**) Entropy (**b**) Mean alpha

Figure 9. Cloude–Pottier decomposition results in a scale from red (high) to blue (low) for the orthogonal vessel at a medium incidence angle (@ ASI 2022).

The Yamaguchi Y4R decomposition reveals the dominance of single-bounce scattering in the two acquisitions when the vessel was oriented orthogonally (Table 9, Figure 10). Double-bounce scattering varies to a great extent. Volume and helix scattering do not contribute significantly in any section of the inflatable.

Table 9. Yamaguchi Y4R decomposition (dimensionless, comparative quantities, normalized to 0->1).

	Helix	Single Bounce	Volume	Double Bounce
Low inc. angle, inclined vessel	0.00	0.07	0.01	0.49
Low inc. angle, orthogonal vessel	0.00	0.48	0.01	0.00
Medium inc. angle, orthogonal vessel	0.00	0.80	0.01	0.39

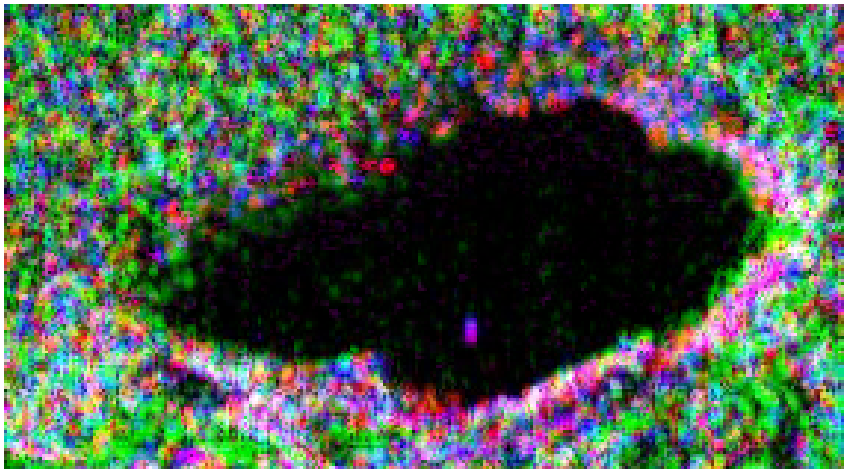

Figure 10. Yamaguchi Y4R RGB-composite showing symmetric (red), irregular/double-bounce (green) and non-symmetric (blue) scattering of the orthogonal vessel at a medium incidence angle (@ ASI 2022).

According to the Cameron decomposition (Table 10), the inflatable is dominated by scattering from dipoles with minor contributions from narrow diplanes and scattering from cylinders. It appears that $\frac{1}{4}$ wave device scattering contributes more at low incidence angles. Trihedral scattering plays a minor role. Asymmetric helix scattering only contributes to a minor extent. There is no direct and simple explanation for the occurrence of these mechanisms; however, they could be related to multiple interactions (in the resolution cell) between the pellet sacks and the water underneath.

Table 10. Cameron decomposition (dimensionless, comparative quantities, normalized to 0->1).

	Trihedral	Dipole	Narrow Diplane	Diplane	Cylinder	1/4 Wave Device	Left Helix	Right Helix
low inc. angle, inclined vessel	0.08	0.47	0.17	0.07	0.26	0.18	0.03	0.01
low inc. angle, orthogonal vessel	0.15	0.53	0.22	0.06	0.11	0.21	0.02	0.01
medium inc. angle, orthogonal vessel	0.06	0.57	0.15	0.06	0.23	0.10	0.00	0.00

All four decompositions show a dominance of surface scattering and double-bounce scattering. Pauli and Cloude–Pottier show that the entropy is at a medium level since, with double-bounce and single-bounce scattering, there are two dominant mechanisms. The result of the Yamaguchi decomposition show an unequal distribution of single-bounce and double-bounce scattering and no double-bounce scattering in one acquisition. This agrees with the Cameron decomposition in showing very little asymmetric helix scattering.

3.3. Detector Testing

The first results are a comprehensive comparison of the performance of nine detectors for three different categories of incidence angles and three different polarization channel combinations. Here, we used the simulated data that combine acquisitions over the sea and the lake. Figure 5 shows an example of a sea truth mask after embedding the boat into the ocean background.

We tested the detectors with two different boat orientations and using all the combinations of these sensor parameters with different wave directions and wave heights, according to the availability of ocean data as listed in Table 4).

For dual co-pol data, most detectors performed worse with increasing H_s and decreasing incidence angles. Very interestingly, the PolEntropy had increasing, or at least stable, AUCs for higher sea states. The fact that it searches for high entropy shows that the entropy of the water surface declines with increasing H_s. This is mostly due to noise floor issues where low sea states produce high entropy backscattering that is close to the noise floor. A high incidence angle can reduce the backscattering even below the noise floor. That is why the PolEntropy detector is the only detector with very low performance at high incidence angles and for calm water surfaces (Figure 11g,h).

The detector performance for HV HH polarization (Figure 12) reveals good and stable performances for most of the detectors at medium incidence angles. The entropy here seems to be less reliable for higher sea states than it is for co-pol data.

In VH VV (Figure 13), the detector performance seems to be less dependent on H_s. The SubCorr and the PolEntropy are not able to match the PWF, the PMF and the PolSym.

Summing up the behaviour of the entropy of the water surface for different polarizations shows that:

- HH VV: the water surface has lower entropy values than the boat except for low sea states and/or high incidence angles.
- HV HH: medium angles: the entropy of the water stays higher than that of the boat; high angles: the entropy of water stays higher than that of the boat.
- VH VV: the entropy of water is lower than that of the boat.

In the following section, one table compares the mean AUCs of all detectors, the next explores the detector performance at higher sea states, and the last visualizes the influence of different boat orientations. They also give an indication of the overall influence of the incidence angle and the polarization.

Table 11 compares the overall performance of all detector algorithms. The best detectors, on average, are the PWF, the PMF and the PolSym. Low incidence angles are not a good choice when it comes to maritime object detection, since increased backscattering from the water surface decreases the TCR. Medium and high incidence angles are more useful for our task. The comparison of combinations of polarizations is strongly biased by different sets of wave heights; for example, the category for medium incidence angles in HV HH does not include any data with high waves.

The same is true for high incidence angles in VH VV. Nevertheless, we see that all three combinations of polarization enable detectors to reach high AUCs.

As Table 12 shows, only results for data with a SPAN greater than -17 dB, it shows that the PMF, the PWF and the PolSym adapt more readily to high sea states. The entropy is more suitable for challenging situations, such as low incidence angles or high seas (high SPAN) at HH VV. For cross-pol, the PolSym seems to be a good choice, and the CACFAR_HH delivers very good results at high incidence angles. Again, all three combinations enable the detectors to deliver comparably good performances on average. When the SPAN reaches over -5 dB, all detectors except PMF, PWF and entropy fall to a level equivalent to random choice (AUC 0.5).

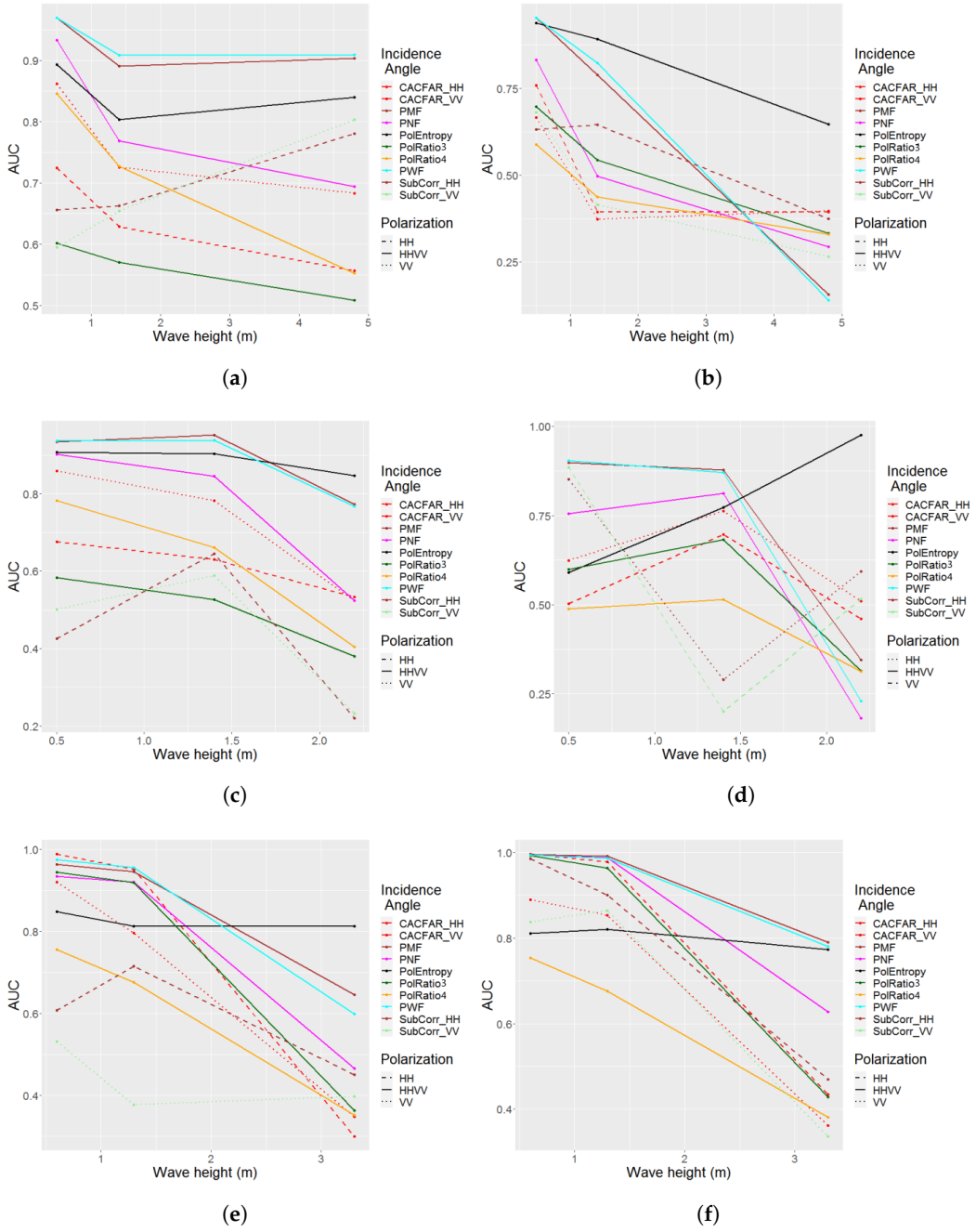

Figure 11. *Cont.*

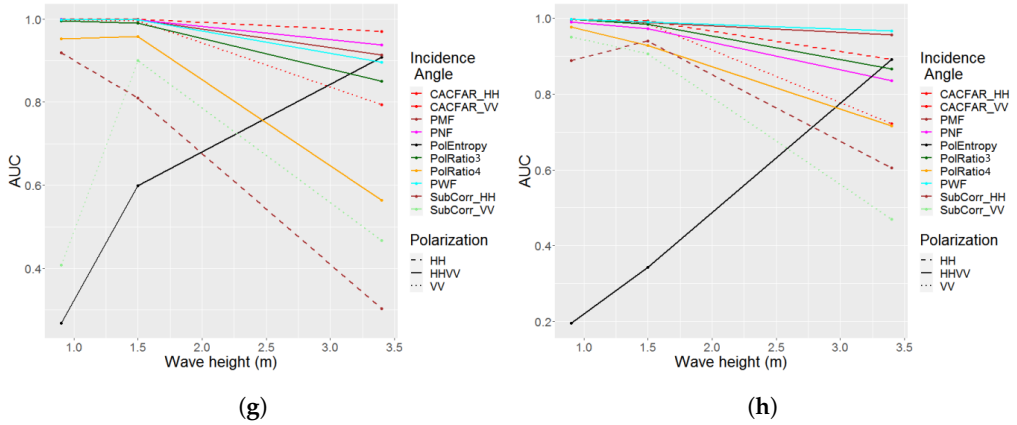

Figure 11. Comparison of the detector AUCs for different wave heights for HH VV. (**a**) Wind: cross, incidence angle: low and boat orientation: 45°. (**b**) Wind: cross, incidence angle: low and boat orientation: 90°. (**c**) Wind: up/down, incidence angle: low and boat orientation: 45°. (**d**) Wind: up/down, incidence angle: low and boat orientation: 90°. (**e**) Wind: up/down, incidence angle: medium and boat orientation: 45°. (**f**) Wind: up/down, incidence angle: medium and boat orientation: 90°. (**g**) Wind: up/down, incidence angle: high and boat orientation: 45°. (**h**) Wind: up/down, incidence angle: high and boat orientation: 90°.

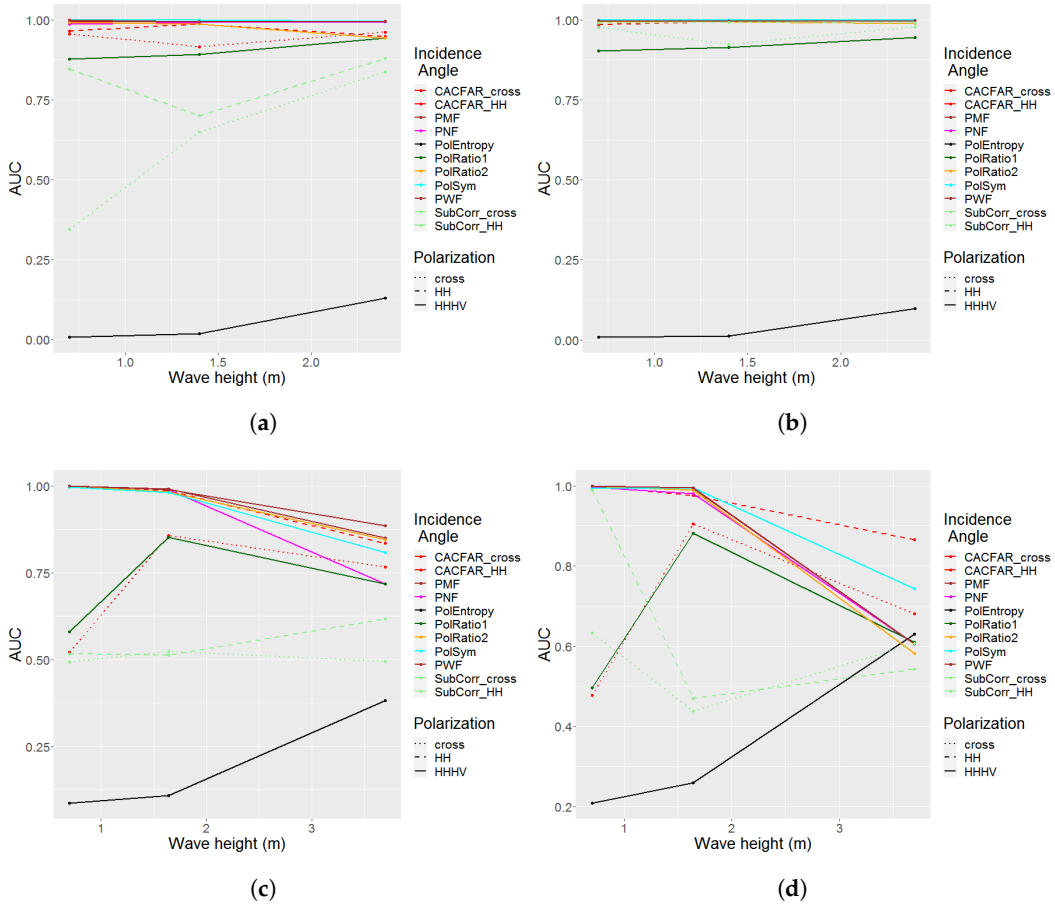

Figure 12. Comparison of the detector AUCs for different wave height for HV HH. (**a**) Wind: up/down, incidence angle: medium and boat orientation: 45°. (**b**) Wind: up/down, incidence angle: medium and boat orientation: 90°. (**c**) Wind: up/down, incidence angle: high and boat orientation: 45°. (**d**) Wind: up/down, incidence angle: high and boat orientation: 90°.

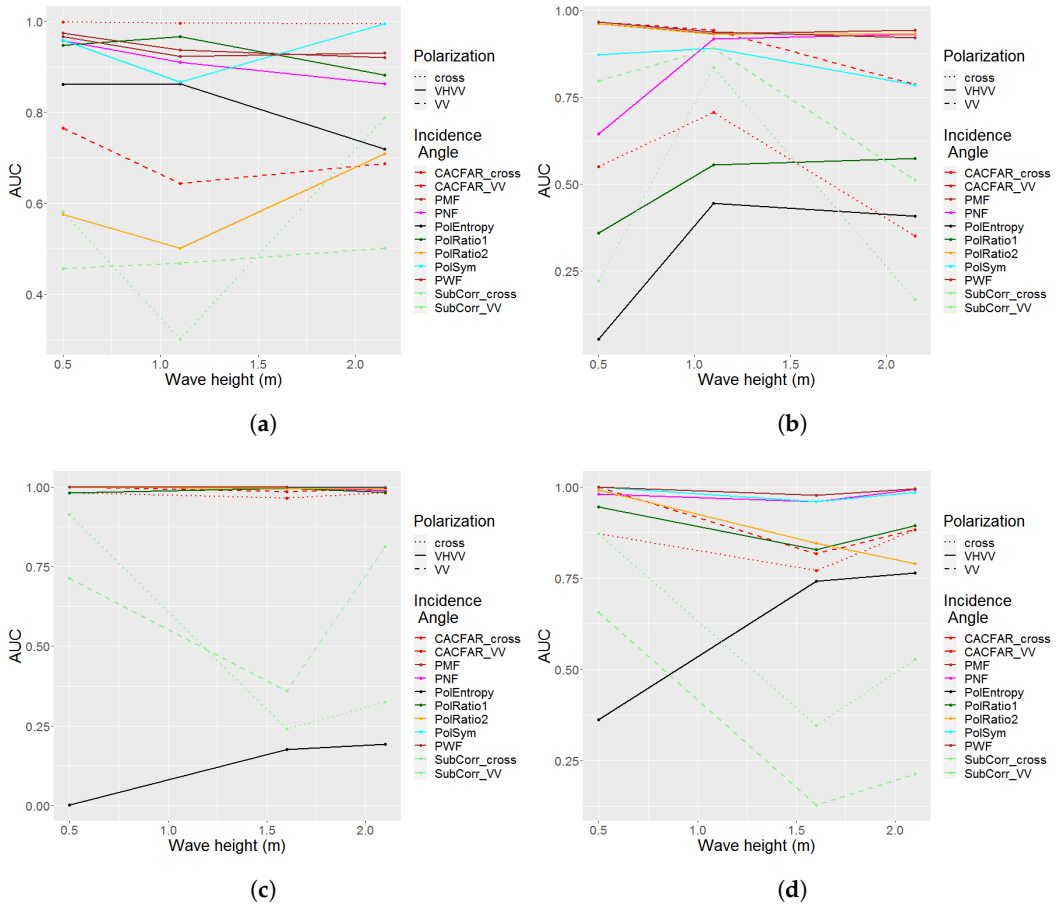

Figure 13. Comparison of the detector AUCs for different wave heights for VH VV. (**a**) Wind: up/down, incidence angle: medium and boat orientation: 45°. (**b**) Wind: up/down, incidence angle: medium and boat orientation: 90°. (**c**) Wind: up/down, incidence angle: high and boat orientation: 45°. (**d**) Wind: up/down, incidence angle: high and boat orientation: 90°.

Table 11. The AUCs of the vessel-detection algorithms with different sensor parameters. The background colours indicate different AUCs from white (low AUCs) to dark green (very high AUCs).

Polarization		**HH VV**		**HV HH**		**VH VV**		
Incidence Angle	**Low**	**Medium**	**High**	**Medium**	**High**	**Medium**	**High**	**Avg**
PMF	0.787	0.888	0.976	0.996	0.906	0.945	0.995	**0.928**
PWF	0.779	0.882	0.975	0.997	0.912	0.941	0.995	**0.926**
PNF	0.670	0.822	0.956	0.994	0.881	0.871	0.986	**0.883**
PolEntropy	0.834	0.813	0.534	0.046	0.279	0.559	0.373	**0.491**
PolRatio1	0.529	0.768	0.947	0.913	0.689	0.714	0.939	**0.786**
PolRatio2	0.554	0.599	0.849	0.983	0.900	0.768	0.936	**0.799**
SubCorr_HH	0.565	0.688	0.744	0.900	0.608			**0.701**
SubCorr_VV	0.528	0.557	0.684			0.604	0.481	**0.571**
SubCorr_cross				0.785	0.531	0.483	0.537	**0.584**
CACFAR_HH	0.600	0.775	0.975	0.980	0.943			**0.854**
CACFAR_VV	0.628	0.695	0.915			0.798	0.946	**0.797**
CACFAR_cross				0.972	0.701	0.766	0.909	**0.837**
PolSym				0.999	0.920	0.895	0.991	**0.951**
avg	**0.647**	**0.749**	**0.856**	**0.869**	**0.752**	**0.759**	**0.826**	

Table 12. The AUCs of the vessel-detection algorithms with high sea states (SPAN > −17 dB). The background colours indicate different AUCs from white (low AUCs) to dark green (very high AUCs).

Polarization		**HH VV**		**HV HH**		**VH VV**		
Incidence Angle	**Low**	**Medium**	**High**	**Medium**	**High**	**Medium**	**High**	**Avg**
PMF	0.787	0.843	0.935		0.728	0.945		**0.848**
PWF	0.779	0.830	0.932		0.745	0.941		**0.846**
PNF	0.670	0.750	0.887		0.662	0.871		**0.768**
PolEntropy	0.834	0.804	0.900		0.506	0.559		**0.721**
PolRatio1	0.529	0.669	0.858		0.664	0.714		**0.687**
PolRatio2	0.554	0.521	0.640		0.714	0.768		**0.639**
SubCorr_HH	0.565	0.634	0.455		0.580			**0.558**
SubCorr_VV	0.528	0.494	0.468			0.604		**0.523**
SubCorr_cross					0.551	0.483		**0.517**
CACFAR_HH	0.600	0.666	0.931		0.850			**0.762**
CACFAR_VV	0.628	0.590	0.758			0.798		**0.694**
CACFAR_cross					0.723	0.766		**0.745**
PolSym					0.776	0.895		**0.835**
avg	**0.647**	**0.680**	**0.776**		**0.682**	**0.759**		

Table 13 shows which detectors and sensor parameters deliver better AUCs for the boat when oriented at 45° (blue) or at 90° (orange) relative to the LoS. In general, the two different experimental setups deliver very comparable results, which backs the theory that the inflatable itself is effectively invisible to microwaves and does not scatter at all. This shows, moreover, that the most dominant scatterers are the passengers whose scattering behaviour is less dependent on the orientation. For low incidence angles in HH VV, the inclined boat is more easily detectable for most detectors. At medium angles, an orthogonal vessel seems to be slightly favourable. At high angles, the boat orientation has no impact at all.

Detectors that use using the cross-pol element (CACFAR_cross, PolRatio1) work slightly better with an inclined boat. The PolRatio1 is, when applied to VH VV or HV HH, called iDPolRAD. The SubCorr is the only detector for which an orthogonal vessel is preferable.

Table 13. The AUCs of the vessel-detection algorithms with different orientations of the rubber vessel. The blue background colours indicate better AUCs for the 45° inclined vessel, the orange colours show higher AUCs for the vessel oriented at 90°.

Polarization		**HH VV**		**HV HH**		**VH VV**		
Incidence Angle	**Low**	**Medium**	**High**	**Medium**	**High**	**Medium**	**High**	**Avg**
PMF	0.23	−0.07	−0.01	0.00	0.08	0.00	0.01	**0.03**
PWF	0.25	−0.08	−0.02	0.00	0.09	0.00	0.01	**0.04**
PNF	0.22	−0.10	0.05	−0.01	0.04	0.08	0.02	**0.04**
PolEntropy	0.06	0.02	0.12	0.01	−0.17	0.51	−0.50	**0.01**
PolRatio1	0.00	−0.05	0.00	−0.02	0.05	0.44	0.10	**0.07**
PolRatio2	0.22	−0.01	−0.05	−0.02	0.09	−0.35	0.12	**0.00**
SubCorr_HH	0.00	−0.19	−0.13	−0.18	−0.12			**−0.13**
SubCorr_VV	0.07	−0.24	−0.18			−0.26	0.30	**−0.06**
SubCorr_cross				−0.35	−0.06	0.15	−0.09	**−0.09**
CACFAR_HH	0.05	−0.06	0.03	−0.03	−0.01			**0.00**
CACFAR_VV	0.22	−0.01	0.03			−0.20	0.09	**0.03**
CACFAR_cross				−0.06	0.03	0.46	0.14	**0.14**
PolSym				0.00	0.02	0.09	0.02	**0.03**
avg	**0.13**	**−0.08**	**−0.02**	**−0.06**	**0.00**	**0.08**	**0.02**	**0.01**

3.4. Detector Fusion

Combining detectors can increase the detection performance. We attempted to find the best combination of detectors for dual-pol cross-pol (VH VV and HV HH) and dual-pol co-pol (HHVV) data separately. In the cross-pol case, we tested the combination of

PolRatio1 and PolRatio2. We used the logical operator 'OR' and called it PolRatioOR. This detector reaches an average AUC of 0.91.

Thus, this 'surface or volume anomaly detector' approaches the best-performing algorithms PolSym and PWF (Figure 14). The PMF reaches similar results, such as those of the PWF, and since their mechanisms are quite similar, we used only the PWF for this comparison. To further increase its performance, we tested various combinations of the PolRatioOR, the PolSym, the PWF and the CACFAR but without any further increase in the AUC.

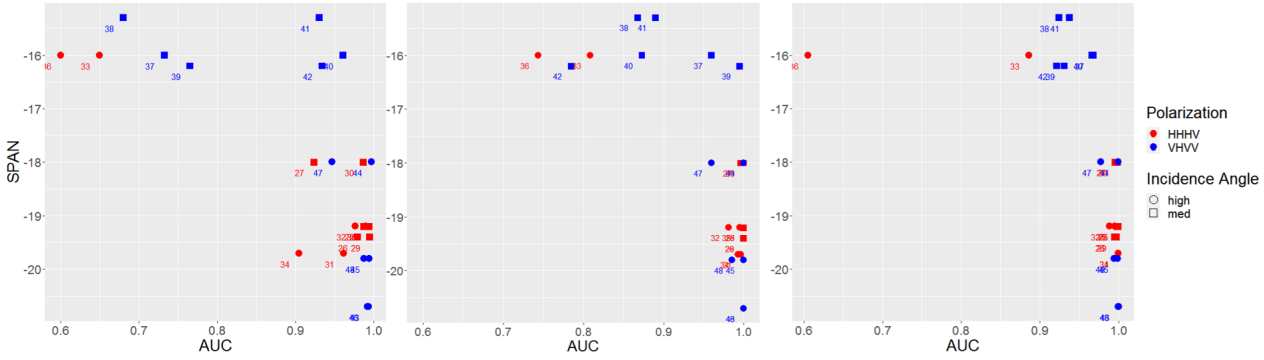

(**a**) (**b**) (**c**)

Figure 14. Comparison of the mean AUCs for different wave heights at VH VV and HV HH for PolRatioOR, PolSym and PWF. (**a**) PolRatioOR ($\overline{AUC}$: 0.91). (**b**) PolSym ($\overline{AUC}$: 0.951). (**c**) PWF ($\overline{AUC}$: 0.961).

The ROC curves for the HV HH dual cross-pol data reveal that wave heights larger than three metres significantly hamper the detection of the inflatable (Figure 15). If we only look at acquisitions taken at a medium incidence angle, a P_d of 90% is possible with a maximum P_{fa} of 0.11%. These results cover wave heights of up to 2.4 metres or BFT6.

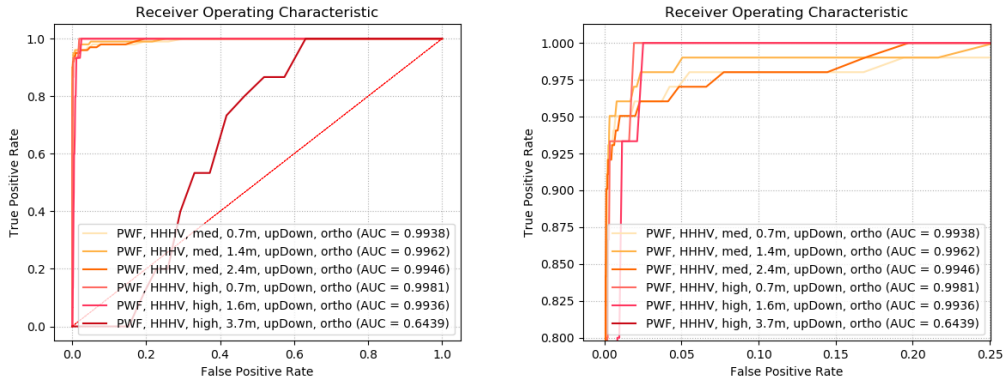

(**a**) (**b**)

Figure 15. ROC curves of the PWF detector for HV HH data with different sea states and the vessel oriented orthogonally to the LoS. (**a**) ROC of PWF overview; (**b**) ROC of PWF zoomed.

The tests with VH VV dual cross-pol imagery give the impression that the PWF delivers better results at high incidence angles (Figure 16). Since the results are partly incoherent, it is difficult to express a recommendation regarding the wave height. The best results for the 90% detection rate were found for a wave height of 0.5 metres with a P_{fa} of 0.12% and for 2.1 metres with a P_{fa} of 1.07%.

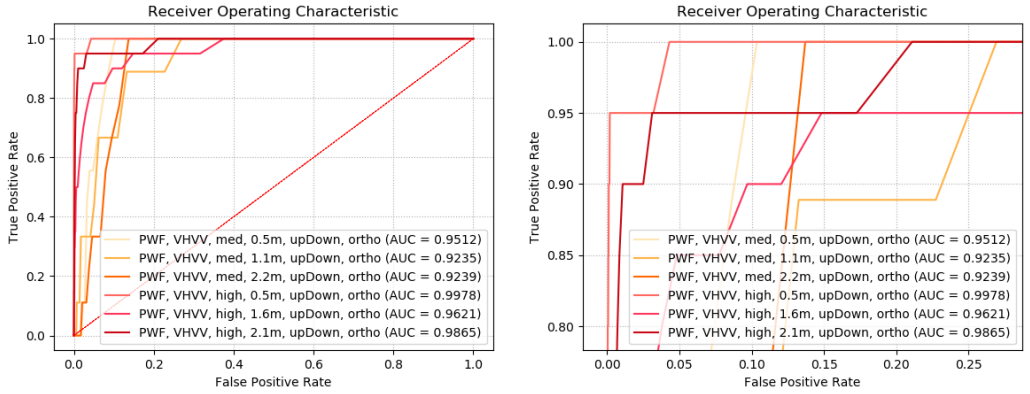

(**a**) (**b**)

Figure 16. ROC curves of the PWF detector for VH VV data with different sea states and the vessel oriented orthogonally to the LoS. (**a**) ROC of PWF overview. (**b**) ROC of PWF zoomed.

In the co-pol case (HH VV), we tested the combinations of a new double-bounce detector ('T_{22}'), PolEntropy, PWF and CACFAR. Again, we left out the PMF due to its very similar performance results. The T_{22} yielded an average AUC of 0.914 for HH VV data, thus, making it the best detector—closely ahead of PMF and PWF, each with an AUC of 0.909.

For our co-pol data (HH VV), the combination using the 'AND' operator for T_{22} and PolEntropy, which we called HT22AND, reached the highest AUC (Figure 17). In particular, the results for higher sea states/higher SPANs are promising. This effect can be attributed to the PolEntropy algorithm.

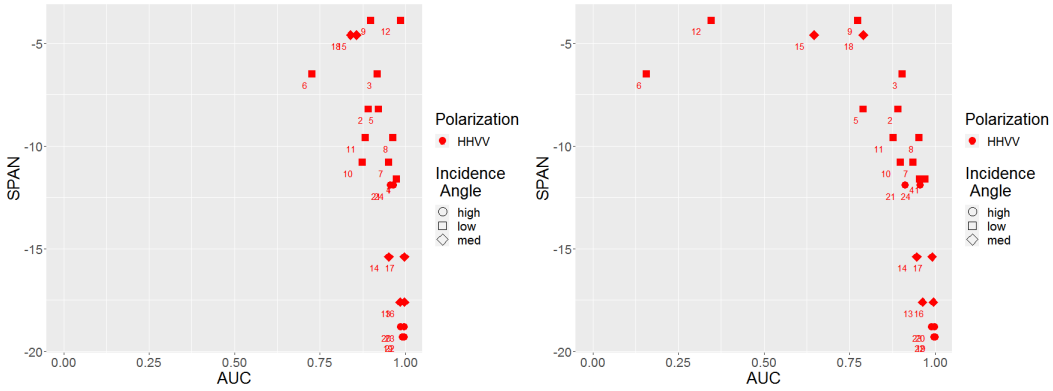

(**a**) (**b**)

Figure 17. Comparison of the mean AUCs for different wave heights at HH VV for HT22AND and PWF. (**a**) HT22AND ($\overline{AUC}$: 0.936). (**b**) PMF ($\overline{AUC}$: 0.884).

Figure 18a helps to describe the predictive strength of the HT22AND detector. We see very poor detection results at low incidence angles (P_{fa} 20% at a P_d of 80%). The same is true for wave heights in the range of three metres, with comparably high false alarm rates. If we look at medium and high incidence angles and wave heights below 1.5 m, the HT22AND reaches a P_d of 90% with a much better P_{fa} of, at most, 0.59% (Figure 18b).

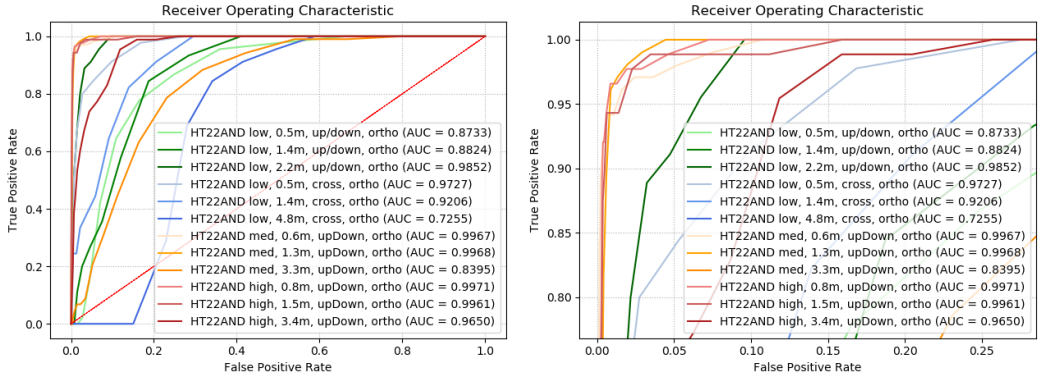

(**a**) (**b**)

Figure 18. ROC curves of the HT22AND detector for HH VV data with different sea states and the vessel oriented orthogonally to the LoS. (**a**) HT22AND overview. (**b**) HT22AND zoomed.

3.5. Estimation of the Detection Quality

These detection results always include some inherent degree of uncertainty. A metric that gives an estimation of the detection quality would be of great help for the sea rescue teams on the ground. Two appropriate parameters for such a metric would be the estimated vessel size and the TCR. These help with the exclusion of large and strong scatterers, such as large metallic ships. Long high waves could have a TCR similar to the inflatable but could be excluded from the positive true list by virtue of their sheer size. Figure 19a shows that the TCR ranges between two and six times the standard deviation of the clutter of the lake. From the TCR, expressed in terms of the standard deviation of the background clutter, a contrast parameter could be calculated (as in [50], called 'significance').

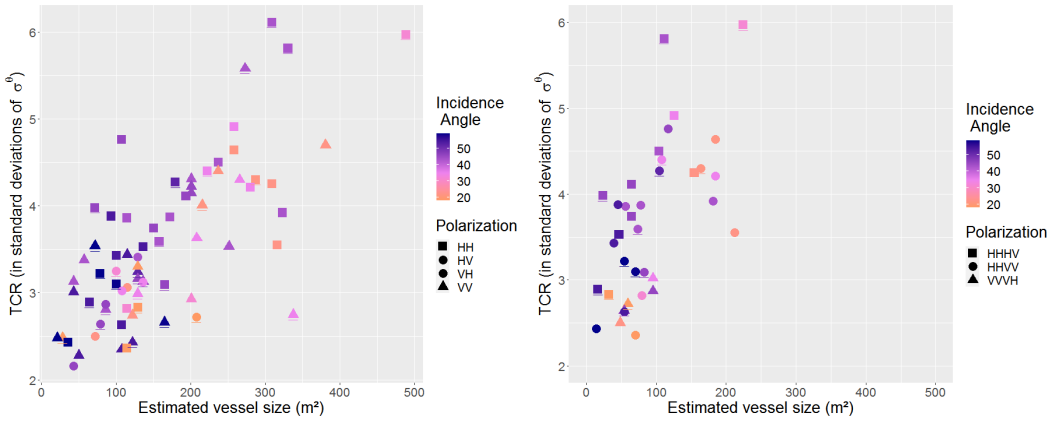

(**a**) (**b**)

Figure 19. Detection quality estimation parameters TCR and estimated vessel size on the lake test bed. (**a**) Polarization channels shown individually. (**b**) Mean values of the two respective coherent dual-pol channels.

The vessel size estimations in our data range from 30 to 500 m² (the true size is 42 m²). Low incidence angles seem to increase the overestimation. If only high incidence angles were used, the variation in estimations reduced to between 30 and 180 m². Figure 19a further reveals a linear correlation between the TCR and the vessel size estimation. Underlined symbols stand for an orthogonal orientation of the boat, the others mean the boat is inclined at 45° and the vessel orientation appears to have no significant impact on the detection quality.

The size estimation can be improved by using the mean value of the two dual-pol channels and by the application of a resizing formula from our previous work [23]. Now, the improved size estimations range between 20 and 250 m²; for high incidence angles,

they stay below 100 m² (Figure 19b). Future work on this could include an analysis of the behaviour of the TCR against the background of different sea states.

4. Discussion

In our approach, we combined maritime SAR data with a simulated fully occupied inflatable by pasting the vessel pixels into the ocean background. That enabled us to create test data that very closely resemble the real situation. The main assumptions that we made in this operation were that:

- The resolution was high enough to resolve the boat pixels separately from the ocean to a large extent.
- The interactions between the vessel and the water surface (flattening of the water surface below the vessel and those caused by the wind shadow on the lee side) were the same in our simulation and in the real situation.
- The wetness of the boat (salty spray on the inflatable and water inside the boat were the same in our simulation and in the real situation.

As a minor effect, we neglected the fact that the rolling of the boat on the ocean (yaw, pitch and roll) induced by waves might change the backscattering of the vessel. Further, the definition of positive true was achieved using the intensity values. That approach biases all results as it helps the intensity-based detectors to perform better compared to the others.

Another noteworthy difference is that the refugee vessel may be moving, even if very slowly. This movement of the vessel triggers certain interactions with the water surface. Since our database has only SAR imagery of a stationary vessel, we could not use and test the movement as a detection mechanism. Therefore, methods, such as along track interferometry (ATI; [51]), which attempt to discriminate non-moving from moving contributions by estimating a velocity-dependent attribute, could be used in the future to improve the effectiveness of migrant boat detection.

Future work could focus on testing the influence of spatial resolution on the different fusion strategies that we proposed. Further, different SAR frequencies (e.g., L-band and C-band) should be added to the test dataset. As mentioned above, the ground truth masks that we used may be improved by exploiting more detectors. Finally, the detectors presented here would gain more confidence if we were able to test them against data with real ground truth obtained from refugee boats.

5. Conclusions

In this work, we attempted to identify the best-performing detectors for a simulated fully occupied refugee inflatable in different weather conditions. For this task, we explored different X-band SAR data types, including TerraSAR-X (TSX), ICEYE and Cosmo-SkyMed Second Generation.

In a preliminary step, we conducted experiments with a ground SAR system to identify bags of wet clay pebbles to simulate humans in SAR. The data acquisition campaign setting was to use these bags to simulate the backscattering of 80 passengers in two different boat orientations (relative to the sensor line of sight) on a lake test bed. Additionally, we created a collection of dual co-pol (HH VV) and dual cross-pol TSX Stripmap data (HV HH and VH VV) from the open ocean with a variety of incidence angles, wave heights and wave directions. We combined the two collections to create a detector testing environment as close as possible to the real situation.

This enabled us to test existing detectors and to develop new variants that were specifically tailored for our rubber inflatable. To further increase the detection capabilities, we experimented with different combinations of detectors.

For dual cross-pol data, we tested a new combination of the volume-detecting Intensity Dual-Polarization Ratio Anomaly Detector (iDPolRAD) and its surface-detecting variant. It reached an overall area under the curve (AUC) of 0.91. For dual co-pol data, the combination of our volume-scattering detector with the polarimetric entropy detector (HT22AND) delivered the best results with an overall AUC of 0.94. The latter is especially interesting,

since it seems to be less compromised by high sea states, and this is mainly caused by the polarimetric entropy detector. A deeper analysis of the best detectors resulted in a better estimation of their capabilities:

- With dual cross-pol channel combinations, the polarimetric whitening filter (PWF) was the best-performing detector.
- With HV HH, the PWF reached, at medium incidence angles, a detection rate of 90% with only 0.12% false detections. Our data support the assumption that the PWF can be used up to a maximum wave height of about 2.4 metres.
- With VH VV data, the PWF had a false detection rate of 1.07% at a 90% detection rate and up to 2.1 m wave height.
- For dual co-pol data, the HT22AND was the best detection algorithm with a false alarm rate of 0.59% at a detection rate of 90%. This is true for wave heights of up to 1.5 m and medium or high incidence angles.

The polarimetric match filter (PMF) delivered equivalent results to those of the PWF throughout all our test data. Although the false alarm rates presented here are not yet good enough to support an efficient detection system for high sea states, the study builds a basis for further research and development. For example, the false alarm rate could be lowered with the help of spatial filters that exclude single pixels as well as very large and very bright false detections.

Author Contributions: Conceptualization, data curation, formal analysis, visualization and methodology: P.L., A.M. and M.D.S.; Funding acquisition: P.L., A.M., T.B., F.K. and M.M.; Investigation: P.L. and A.M.; Project administration: P.L., T.B. and F.K.; Resources, A.M., T.B., F.K. and M.M.; Software and validation: P.L. and A.M.; Supervision, A.M., T.B., F.K. and M.M.; Writing—original draft, P.L.; Writing—review and editing, A.M. All authors have read and agreed to the published version of the manuscript.

Funding: This document is a result of the PhD program Safe Automation of Maritime Systems (SAMS) funded by the state of Lower Saxony and the internal research fund of the Jade University Oldenburg.

Informed Consent Statement: Informed consent was obtained from all subjects involved in the study.

Data Availability Statement: We used the following publicly archived datasets for in situ weather data: The Copernicus Marine Environment Monitoring Service at https://marine.copernicus.eu/, accessed on 30 March 2023. The Copernicus Marine Environment Monitoring Service In Situ Thematic Assembly Centre at https://marine.copernicus.eu/about/producers/insitu-tac, accessed on 30 March 2023.

Acknowledgments: We would like to thank all the people who have supported the theoretical and experimental/practical work described in this paper. We would also like to thank the German Aerospace Center DLR, the Agenzia Spaziale Italiana ASI and ICEYE as they provided friendly cooperation and the satellite data. Special thanks goes to the Wokule community who made the satellite data campaign a wonderful experience.

Conflicts of Interest: The authors declare no conflict of interest.

References

1. IOM. Missing Migrants Project. Available online: https://missingmigrants.iom.int/region/mediterranean (accessed on 23 March 2023).
2. IOM. Displacement Tracking Matrix. Available online: https://dtm.iom.int/europe/arrivals (accessed on 23 March 2023).
3. UNHCR. Mediterranean Situation. Available online: https://data.unhcr.org/en/situations/mediterranean (accessed on 23 March 2023).
4. Novak, L.M.; Sechtin, M.B.; Burl, M.C. *Algorithms for Optimal Processing of Polarimetric Radar Data*; Polarimetric Technology Handbook, GACIAC HB 92–01, 139–206, Chicago; Massachusetts Institute of Technology Lexington Lincoln Lab: Lexington, MA, USA, 1989; p. 99.
5. Crisp, D.J.; Redding, N.J. Ship Detection in Synthetic Aperture Radar Imagery. In Proceedings of the 12th Australasian Remote Sensing and Photogrammetry Conference, Fremantle, Australia, 18–22 October 2004; p. 10.

6. Liu, C.; Vachon, P.W.; Geling, G.W. Improved Ship Detection Using Polarimetric SAR Data. In Proceedings of the IGARSS 2004, 2004 IEEE International Geoscience and Remote Sensing Symposium, Anchorage, AK, USA, 20–24 September 2004; Volume 3, pp. 1800–1803. [CrossRef]
7. Yeremy, M.; Campbell, J.W.M.; Mattar, K.; Potter, T. Ocean Surveillance with Polarimetric SAR. *Can. J. Remote Sens.* **2001**, *27*, 328–344. [CrossRef]
8. Touzi, R.; Charbonneau, F.; Hawkins, R.K.; Murnaghan, K.; Kavoun, X. Ship-Sea Contrast Optimization When Using Polarimetric SARs. In Proceedings of the IGARSS 2001, Scanning the Present and Resolving the Future, Proceedings, IEEE 2001 International Geoscience and Remote Sensing Symposium (Cat. No. 01CH37217), Sydney, Australia, 9–13 July 2001; Volume 1, pp. 426–428.
9. Marino, A. A Notch Filter for Ship Detection with Polarimetric SAR Data. *IEEE J. Sel. Top. Appl. Earth Obs. Remote Sens.* **2013**, *6*, 1219–1232. [CrossRef]
10. Marino, A.; Sugimoto, M.; Nunziata, F.; Hajnsek, I.; Migliaccio, M.; Ouchi, K. Comparison of Ship Detectors Using Polarimetric Alos Data: Tokyo Bay. In Proceedings of the 2013 IEEE International Geoscience and Remote Sensing Symposium (IGARSS), Melbourne, Australia, 21–26 July 2013; pp. 2345–2348.
11. Nunziata, F.; Migliaccio, M.; Brown, C.E. Reflection Symmetry for Polarimetric Observation of Man-Made Metallic Targets at Sea. *IEEE J. Ocean. Eng.* **2012**, *37*, 384–394. [CrossRef]
12. Kang, M.; Ji, K.; Leng, X.; Lin, Z. Contextual Region-Based Convolutional Neural Network with Multilayer Fusion for SAR Ship Detection. *Remote Sens.* **2017**, *9*, 860. [CrossRef]
13. Zhao, J.; Guo, W.; Zhang, Z.; Yu, W. A Coupled Convolutional Neural Network for Small and Densely Clustered Ship Detection in SAR Images. *Sci. China Inf. Sci.* **2019**, *62*, 42301. [CrossRef]
14. Girshick, R.; Donahue, J.; Darrell, T.; Malik, J. Rich Feature Hierarchies for Accurate Object Detection and Semantic Segmentation. In Proceedings of the 2014 IEEE Conference on Computer Vision and Pattern Recognition, Columbus, OH, USA, 23–28 June 2014; pp. 580–587. [CrossRef]
15. Girshick, R. Fast R-Cnn. In Proceedings of the IEEE International Conference on Computer Vision, Santiago, Chile, 7–13 December 2015; pp. 1440–1448.
16. Ren, S.; He, K.; Girshick, R.; Sun, J. Faster R-CNN: Towards Real-Time Object Detection with Region Proposal Networks. In *Advances in Neural Information Processing Systems 28*; Cortes, C., Lawrence, N.D., Lee, D.D., Sugiyama, M., Garnett, R., Eds.; Curran Associates, Inc.: Red Hook, NY, USA, 2015; pp. 91–99.
17. Li, J.; Qu, C.; Shao, J. Ship Detection in SAR Images Based on an Improved Faster R-CNN. In Proceedings of the 2017 SAR in Big Data Era: Models, Methods and Applications (BIGSARDATA), Beijing, China, 13–14 November 2017; pp. 1–6. [CrossRef]
18. Zhang, S.; Wu, R.; Xu, K.; Wang, J.; Sun, W. R-CNN-Based Ship Detection from High Resolution Remote Sensing Imagery. *Remote Sens.* **2019**, *11*, 631. [CrossRef]
19. Zhang, T.; Zhang, X. High-Speed Ship Detection in SAR Images Based on a Grid Convolutional Neural Network. *Remote Sens.* **2019**, *11*, 1206. [CrossRef]
20. Redmon, J.; Divvala, S.; Girshick, R.; Farhadi, A. You Only Look Once: Unified, Real-Time Object Detection. In Proceedings of the 2016 IEEE Conference on Computer Vision and Pattern Recognition (CVPR),: Las Vegas, NV, USA, 27–30 June 2016; pp. 779–788. [CrossRef]
21. Chang, Y.L.; Anagaw, A.; Chang, L.; Wang, Y.; Hsiao, C.Y.; Lee, W.H. Ship Detection Based on YOLOv2 for SAR Imagery. *Remote Sens.* **2019**, *11*, 786. [CrossRef]
22. Rostami, M.; Kolouri, S.; Eaton, E.; Kim, K. Deep Transfer Learning for Few-Shot SAR Image Classification. *Remote Sens.* **2019**, *11*, 1374. [CrossRef]
23. Lanz, P.; Marino, A.; Brinkhoff, T.; Köster, F.; Möller, M. The InflateSAR Campaign: Evaluating SAR Identification Capabilities of Distressed Refugee Boats. *Remote Sens.* **2020**, *12*, 3516. [CrossRef]
24. Lanz, P.; Marino, A.; Brinkhoff, T.; Köster, F.; Möller, M. The InflateSAR Campaign: Testing SAR Vessel Detection Systems for Refugee Rubber Inflatables. *Remote Sens.* **2021**, *13*, 1487. [CrossRef]
25. Marino, A.; Dierking, W.; Wesche, C. A Depolarization Ratio Anomaly Detector to Identify Icebergs in Sea Ice Using Dual-Polarization SAR Images. *IEEE Trans. Geosci. Remote Sens.* **2016**, *54*, 5602–5615. [CrossRef]
26. Holt, B. SAR Imaging of the Ocean Surface. In *Synthetic Aperture Radar Marine User's Manual*; Jackson, C., Apel, J., Eds.; NOAA/NESDIS: Washington, DC, USA, 2004; pp. 25–79.
27. Microwaves101. Miscellaneous Dielectric Constants. Available online: https://www.microwaves101.com/encyclopedias/miscellaneous-dielectric-constants (accessed on 15 January 2023).
28. Agency, E.S. Mediterranean Sea Salinity. Available online: https://www.esa.int/ESA_Multimedia/Images/2017/05/Mediterranean_Sea_salinity (accessed on 17 January 2023).
29. Van Zyl, J.J.; Arii, M.; Kim, Y. Model-Based Decomposition of Polarimetric SAR Covariance Matrices Constrained for Nonnegative Eigenvalues. *IEEE Trans. Geosci. Remote Sens.* **2011**, *49*, 3452–3459. [CrossRef]
30. Klein, L.A.; Swift, C.T. An Improved Model for the Dielectric Constant of Sea Water at Microwave Frequencies. *IEEE Trans. Antennas Propag.* **1977**, *25*, 104–111. [CrossRef]
31. Guo, C.; Ye, H.; Zhou, Y.; Xu, Y.; Wang, L. Scaled Sea Surface Design and RCS Measurement Based on Rough Film Medium. *Sensors* **2022**, *22*, 6290. [CrossRef] [PubMed]

32. Hozhabri, M.; Risman, P.O.; Petrovic, N. Comparison of UWB Radar Backscattering by the Human Torso and a Phantom. In Proceedings of the 2018 IEEE Conference on Antenna Measurements & Applications (CAMA), Västerås, Sweden, 3–6 September 2018; pp. 1–4. [CrossRef]
33. Valenzuela, G.R. Theories for the Interaction of Electromagnetic and Oceanic Waves—A Review. *Bound.-Layer Meteorol.* **1978**, *13*, 61–85. [CrossRef]
34. Robinson, I.S. *Measuring the Oceans from Space: The Principles and Methods of Satellite Oceanography*; Springer Science & Business Media: Berlin/Heidelberg, Germany, 2004.
35. Voronovich, A.G.; Zavorotny, V.U. Theoretical Model for Scattering of Radar Signals in Ku- and C-bands from a Rough Sea Surface with Breaking Waves. *Waves Random Media* **2001**, *11*, 247. [CrossRef]
36. Mouche, A.A.; Chapron, B.; Reul, N. A Simplified Asymptotic Theory for Ocean Surface Electromagnetic Wave Scattering. *Waves Random Complex Media* **2007**, *17*, 321–341. [CrossRef]
37. Kudryavtsev, V.; Hauser, D.; Caudal, G.; Chapron, B. A Semiempirical Model of the Normalized Radar Cross-Section of the Sea Surface 1. Background Model. *J. Geophys. Res. Ocean.* **2003**, *108*, FET 2-1–FET 2-24. [CrossRef]
38. Ren, Y.; Lehner, S.; Brusch, S.; Li, X.; He, M. An Algorithm for the Retrieval of Sea Surface Wind Fields Using X-band TerraSAR-X Data. *Int. J. Remote Sens.* **2012**, *33*, 7310–7336. [CrossRef]
39. Weber, J.E.H. Vertically Varying Eulerian Mean Currents Induced by Internal Coastal Kelvin Waves. *J. Geophys. Res. Ocean.* **2017**, *122*, 1222–1231. [CrossRef]
40. Zhang, L.; Zhang, J.; Zou, B.; Zhang, Y. Comparison of Methods for Target Detection and Applications Using Polarimetric SAR Image. In Proceedings of the Progress in Electromagnetics Research Symposium, Hangzhou, China 24–28 March 2008; Volume 1.
41. Cloude, S.R.; Pottier, E. A Review of Target Decomposition Theorems in Radar Polarimetry. *IEEE Trans. Geosci. Remote Sens.* **1996**, *34*, 498–518. [CrossRef]
42. Cloude, S.; Pottier, E. An Entropy Based Classication Scheme for Land Applications of Polarimetric SAR. *IEEE Trans. Geosci. Remote Sens.* **1997**, *35*, 68–78. [CrossRef]
43. Yamaguchi, Y.; Moriyama, T.; Ishido, M.; Yamada, H. Four-Component Scattering Model for Polarimetric SAR Image Decomposition. *IEEE Trans. Geosci. Remote Sens.* **2005**, *43*, 1699–1706. [CrossRef]
44. Freeman, A.; Durden, S.L. Three-Component Scattering Model to Describe Polarimetric SAR Data. In *Proceedings of the Radar Polarimetry*; International Society for Optics and Photonics: Washington, DC, USA, 1993; Volume 1748, pp. 213–224.
45. Kennaugh, E.M.; Sloan, R.W. *Effects of Type of Polarization On Echo Characteristics*; Technical Report; Ohio State Univ Research Foundation Columbus Antenna Lab: Columbus, OH, USA, 1952.
46. Cameron, W.L.; Leung, L.K. Feature Motivated Polarization Scattering Matrix Decomposition. In Proceedings of the IEEE International Conference on Radar, Arlington, VA, USA, 7–10 May 1990; pp. 549–557.
47. Krogager, E. New Decomposition of the Radar Target Scattering Matrix. *Electron. Lett.* **1990**, *26*, 1525–1527. [CrossRef]
48. Karachristos, K.; Anastassopoulos, V. Land Cover Classification Based on Double Scatterer Model and Neural Networks. *Geomatics* **2022**, *2*, 323–337. [CrossRef]
49. Singh, G.; Mohanty, S.; Yamazaki, Y.; Yamaguchi, Y. Physical Scattering Interpretation of POLSAR Coherency Matrix by Using Compound Scattering Phenomenon. *IEEE Trans. Geosci. Remote Sens.* **2020**, *58*, 2541–2556. [CrossRef]
50. Tello, M.; López-Martínez, C.; Mallorqui, J.J. A Novel Algorithm for Ship Detection in SAR Imagery Based on the Wavelet Transform. *IEEE Geosci. Remote Sens. Lett.* **2005**, *2*, 201–205. [CrossRef]
51. Raney, R.K. Synthetic Aperture Imaging Radar and Moving Targets. *IEEE Trans. Aerosp. Electron. Syst.* **1971**, *AES-7*, 499–505. [CrossRef]